ELSEVIER

Contents lists available at ScienceDirect

Thin Solid Films

journal homepage: www.elsevier.com/locate/tsf



Large area pulsed laser deposition of memristive Pr_{0.7}Ca_{0.3}MnO₃ heterostructures for neuromorphic computing

M. Buczek ^{a,*}, M. Pohlmann ^c, Z. Liu ^a, Z. Moos ^a, A. Gutsche ^b, P. Cao ^d, J. Mayer ^d, W. Stein ^c, R. Dittmann ^a

- ^a Forschungszentrum Juelich GmbH, PGI-7, Jülich D-52425, Germany
- ^b Forschungszentrum Juelich GmbH, PGI-10, Jülich D-52425, Germany
- ^c SURFACE systems + technology GmbH + Co KG, Hückelhoven D-41836, Germany
- ^d Forschungszentrum Juelich GmbH, ER-C, Jülich D-52425, Germany

ARTICLEINFO

Keywords:

Large area pulsed laser deposition Pulsed laser deposition Memristive devices Praseodymium calcium manganite Area dependent switching Interface-type resistive switching Neuromorphic computing Resistive random access memories

ABSTRACT

Heterostructures of the perovskite $Pr_{0.7}Ca_{0.3}MnO_3$ (PCMO) and a tunnel oxide such as AlO_x are highly interesting memristive devices for emulating synaptic properties in neuromorphic circuits. Future chip generations with these memristive elements requires PLD systems which enables PCMO growth on a full wafer. To address the issue of plume broadening in this study, a slit system was used to localize the deposition region, thereby eliminating the need for excessive scanning. This study investigates the effect of the slit system and process gas pressure on plume broadening. This investigation has been used to parameterize a simulation software to assess the effectiveness of different movement speeds and to develop strategies for homogeneous deposition, adjustable to a chosen film thickness in the order of twenty nanometers. We used these strategies to fabricate area dependent switching memory cells on a standard $4^{\prime\prime}$ Si wafer using the material combination of $Pr_{0.7}Ca_{0.3}MnO_3$ and AlO_x . The influence of the aluminum oxide thickness on the switching shows that the IV loop starts to exhibit a hysteresis for AlO_x thicknesses ≥ 3 nm. An increase in AlO_x thickness leads to an increase in resistance and capacitive charging. An additional thermal treatment reduces the resistance and the switching voltage and increases the ratio between low resistive and high resistive state. Devices without thermal treatment of the PCMO are compatible for back end of line processing of standard CMOS technology.

1. Introduction

In the field of neuromorphic computing, particularly in the search for alternative computing architectures that avoid the von Neumann bottleneck, there is a strong interest in using alternative types of memory devices. Resistive random-access memories (ReRAMs) are potential candidates [1]. Among the various types of ReRAM, area-dependent switching memory cells offer the advantage that the resistance of the device can be adjusted by the selected device size [2,3]. Moreover, the SET kinetics are not dominated by a thermal runaway effect, as it is the case in competing filamentary devices [4,5]. Therefore, area-dependent memristive devices show gradual switching for both SET and RESET. Among the various possible realizations of area-dependent devices, the combination of praseodymium calcium manganate (PCMO) and AlO $_{\rm X}$ is a promising memristive heterostructure [6-8].

Pulsed laser deposition (PLD) is a well-established technique for the

epitaxial deposition of complex metal oxides in academic research [9, 10]. The deposition is typically performed on small samples $\sim 1~{\rm cm}^2$ in size [11-13]. However, PLD has not yet played a significant role in industrial thin film deposition on large wafers [14,15]. A major issue for large-area deposition is the directional expansion of the plasma plume. Therefore, the effective deposition area is much smaller than a 4" or larger wafer [16]. It is necessary to use a scanning concept that achieves full wafer coverage of the deposited film [15,17].

Each concept should address the following issues: Ensuring a homogenous ablation from the target material by moving the laser spot over the target surface. This is important to avoid distortions of the laser spot and ensure a homogenous and reliable deposition. The coverage of the films by droplets can be a challenge for the application of PLD. To prevent the formation of droplets, it is recommended to use dense targets with a sintering density close to the crystalline density [16] and sharply projected laser spots without local fluctuations of the fluence.

E-mail address: m.buczek@fz-juelich.de (M. Buczek).

^{*} Corresponding author.

The deposition time must be fast enough to meet the economic time requirements of the production process. The fluence control must consider the change in the transmission of the laser entrance window, and the laser entrance window must be easily replaceable [18]. Most importantly, the relative movement between the plume and substrate must stitch the individual deposition plumes together to create a homogeneous film across the entire wafer. This is particularly challenging if the strategy needs to be easily adaptable for different deposition thicknesses, especially when the targeted film thickness is 20 nm or below.

Many different concepts are possible; until today, no single concept is considered the best. Rotating the substrate and scanning the ablation spot over a parallel-positioned target via mirror rotation is popular. The scan range over the target must be well-aligned to the radius of the substrate. Therefore, a homogeneous deposition can be achieved by scanning the laser spot along the target with varying speeds (faster scanning speed towards the center of the substrate) [17,19–21]. A problem of this strategy is that the alternation of the projection angle by the mirror rotation changes the spot size on the target [18], which can influence the deposition rate and the stoichiometry [16]. Addressing this issue, there is a modified concept where the scanning of the laser beam happens at a constant projected angle by a translation movement of the beamline and a target with inclined positions towards the substrate surface [22].

However, the concept of two-dimensional scanning with linear movements is the most direct way to achieve a homogeneous deposition on a wafer. A major issue for this strategy is the broadening of the deposition plume as the distance between the target and substrate increases [23]. This broadening occurs in high vacuum due to plume self-interaction and is significantly increased due to scattering processes when a process gas is used. It is a problem for homogeneity since it causes higher deposition rates in the central areas of the wafer than in the edge areas when the scanning motion doesn't allows much longer movement distances as the wafer is big.

To address the issue of plume broadening in this study, a slit system was used to localize the deposition region, thereby eliminating the need for excessive scanning. The first part of the study investigates the effect of the slit system and process gas pressure on plume broadening. This investigation has been used to parameterize simulation software to assess the effectiveness of different movement speeds and to develop strategies for homogeneous deposition, adjustable to a chosen film thickness in the order of 20 nm. In the second part of this work, we used these strategies to fabricate area-dependent switching memory cells on a standard $4^{\prime\prime}$ Si wafer using the material combination of $Pr_{0.7}Ca_{0.3}MnO_3$ and AlO_x .

2. Experimental methods

A KrF excimer laser is used with a 100 Hz repetition rate to reduce the process time. The high number of shots for a single deposition (order of 100,000 shots per sample) leads to deposition on the laser entrance window, which causes a relevant change in the optical transmission after a few depositions. This effect is stronger with lower process gas pressure. Two features are installed to handle this issue. The first feature is a thin quartz glass slide mounted inside the chamber in front of the entrance window for protection. These slides are getting exchanged by an in-vacuum working magazine system with space for 10 exchange glass slides. Furthermore, the energy measurement for the fluence control includes the change in the transmission of the glass slides. Therefore, the target gets moved to the side during the energy measurement, and the laser beam leaves the chamber through an additional exit window. This exit window is covered during the deposition.

The laser beam is projected onto the target by the beamline, which is mounted entirely on rails to maintain a constant distance throughout the movement. On the beamline, the beam is first slightly focused by a convex lens to correct for the divergence of the excimer beam. Directly behind the lens is the aperture, which shapes the beam profile rectangular with a size of 22 mm x 10 mm The shaped beam is then guided by the two mirrors through two further lenses. First, a divergence lens increases the imaginary distance to the aperture, and then a focusing lens directly in front of the chamber entrance window projects the aperture onto the target. The resulting spot size has a rectangular shape of (2.28 - 2.39) mm x (1.22 - 1.60) mm, with the long side parallel to the cylinder axis, and is taken into account in the fluence control software with an average spot size of 0.034 cm².

The laser ablates a ceramic target, and the resulting plasma plume condenses on the sample surface. The used PCMO target had a density of $4.53~g/cm^3$ (relative density of 86~% [24]), and the used SrTiO₃ (STO) target had a density of 5.06 (relative density of 99~% [25]). The PLD system uses a cylindrical target (see Fig. 1). The deposition process is controlled by two movements: one-dimensional scanning of the substrate and one-dimensional scanning of the laser beam line along the cylindrical surface of the target. The deposition of the full layer is achieved by combining these two movements. Homogeneous ablation of the target surface is achieved by rotating the cylindrical target and combining this with the one-dimensional movement of the laser beam.

To address the issue of plume broadening, a slit system was installed. The two-dimensional scanning consists of movements along two axes. Slits are mounted perpendicular to each axis of motion to confine the plume deposition to the aimed area. One axis is the movement of the substrate itself, which moves behind a fixed slit (Fig. 1a). The slit is called a "heat shield slit" because it also protects the chamber from thermal radiation during high-temperature deposition. The second axis

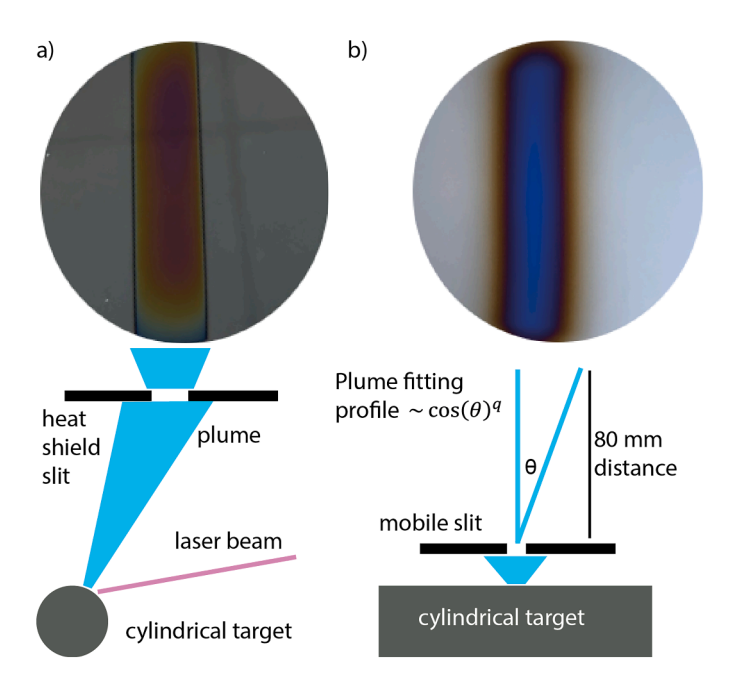


Fig. 1. Slit system for 2-dimensional scanning. **a)** Viewing direction on the cylinder base of the target. Image of a deposited film for exclusive movement of the laser spot, edges given by the heat shield. **b)** Viewing direction on the cylinder surface of the target. Image of a deposited film for exclusive movement of the substrate, edges given by the mobile slit.

is the movement of the laser spot over the cylindrical target. The plume is confined along this axis by a slit that moves with the laser spot in the chamber (Fig. 1b). To achieve this, the entire beamline is mounted on rails and moves during the process while maintaining focus.

The PCMO/AlO_x based memristive devices on the 4" Si wafer (schematic stack visible in Fig. 4c) were fabricated using the following process parameters. The Si wafer was thermally wet oxidized to an oxide thickness of approximately 430 nm SiO₂. On top of this, 5 nm of Ta was sputtered by RF magnetron sputtering, and 25 nm of Pt was deposited by DC magnetron sputtering. The Ta acts as an adhesion layer for the platinum bottom electrode. The PLD deposition of PCMO takes place at room temperature with a fluence of $2.5 \, \text{J/cm}^2$ and an oxygen pressure of 1 Pa. If the sample had a thermal annealing treatment, it was heated after PLD deposition by rapid thermal annealing with IR illumination for 2 min at 923 K under N₂ atmosphere. The AlO_x was deposited by 200 W magnetron RF sputtering of aluminum under a 1 Pa reactive oxygenargon atmosphere (3:2 (Ar:O₂) flow rate mixture). The 20 nm Pt top electrode was deposited by DC magnetron sputtering.

The pad electrodes with three different sizes ($20~\mu m \times 20~\mu m$, $50~\mu m \times 50~\mu m$ and $100~\mu m \times 100~\mu m$) were patterned by optical lithography and structured by dry etching with an argon beam. The common Pt bottom electrode was contacted by wedge bonding. The local pad top electrodes were contacted by flexible Wolfram needles. Electrical characterization was carried out using a Keithley 2611A source measurement unit.

3. Results

3.1. Influence of slit system and working pressure

Fig. 1a shows the image of a deposited film when only the beamline is moving. The edges are defined by the static slit, which is close to the substrate and therefore produces sharp edges. Fig. 1b shows an image of a deposited film when only the substrate is moved. The edges given by

the moving slit close to the target are diffuse. As this slit is further away from the substrate, the confinement function is less pronounced. To tune the deposition, we investigated the influence of the slit further away from the substrate on the deposition profile, as its confinement function is less effective.

First, the influence of slit width and oxygen pressure on the deposition rate was investigated. STO, as standard complex oxide material, was used as the target material to increase the applicability of our investigations to other complex oxides. Fig. 2d shows that the deposition rates, determined by X-ray reflectivity measurements (XRR), are similar for most slit sizes. A noticeable decrease in deposition rate is observed for a slit width of 3.5 mm, which approaches the laser spot width of 2.5 mm. It is also evident that the deposition rate decreases at higher pressures, with vanishing rates above 5 Pa.

3.2. Parameterization of the simulation software

Using the knowledge of the pressure range of interest, we then characterized the deposition profiles of STO for different slit widths at different pressures with XRR and fitted them with the function $\cos\left(a+\tan^{-1}\frac{x}{80\ mm}\right)^q$ where a and q are the fitting parameter and $\tan^{-1}\frac{x}{80\ mm}$ the angle θ for the used substrate- target distance of 80 mm, see Fig. 2 a, c, d. These profiles were then integrated into simulation software from the company *Surface*, which simulates deposition over the entire wafer for selected motion velocities Fig. 3a, c. The simulation is a Python-based grid calculation. For each laser pulse, the positions of all motors will be calculated based on their velocities. On a width equal to the defined slit size around the resulting motor position, the deposition rate profile for the respective pressure and slit size is summed up on the grid. The result is a height distribution, either relative or absolute, depending on whether the deposition profile is given as normalized or nm/laser pulse.

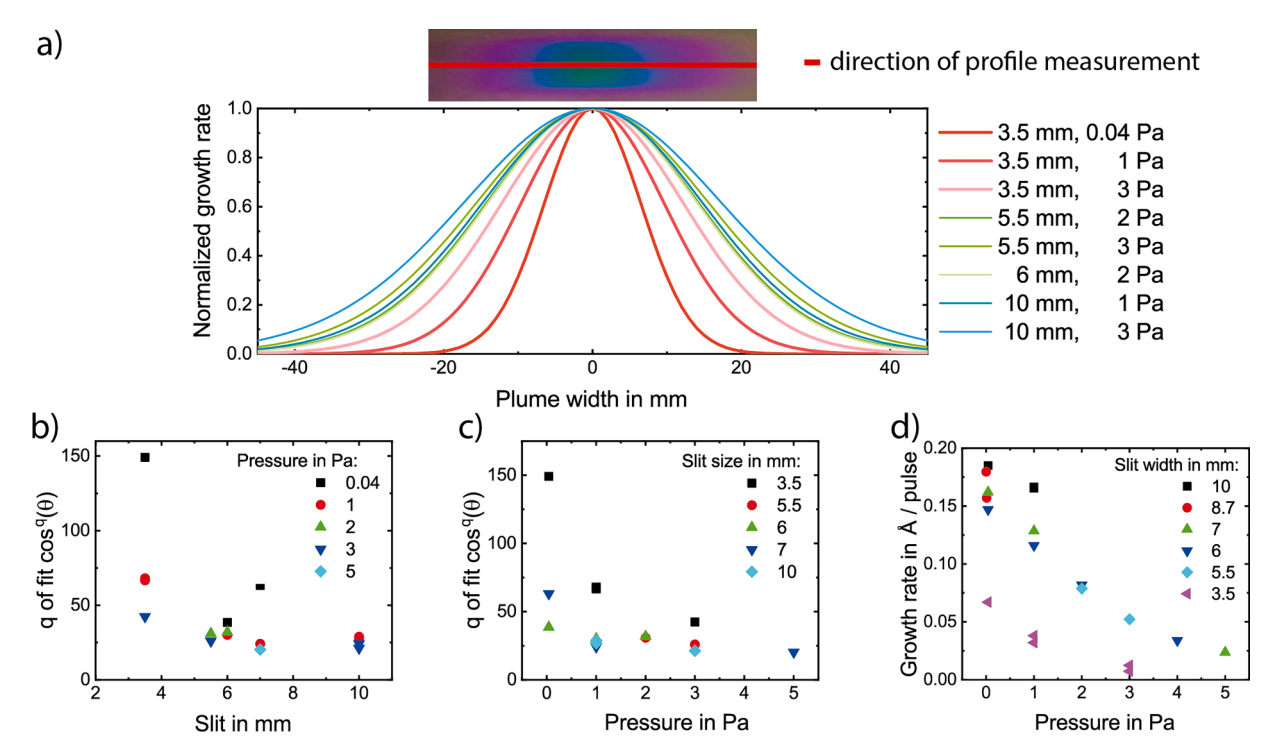


Fig. 2. Deposition rate in dependency of the slit width and the pressure and fitting of the deposition profile. a) Fitted $\cos(\theta)^q$ functions of the STO deposition profiles (measured by XRR). b + c) Fitted q values in dependency of the (b) slit width variation and the (c) O_2 process gas pressure. d) Maximum STO growth rate in dependency of slit width and pressure.

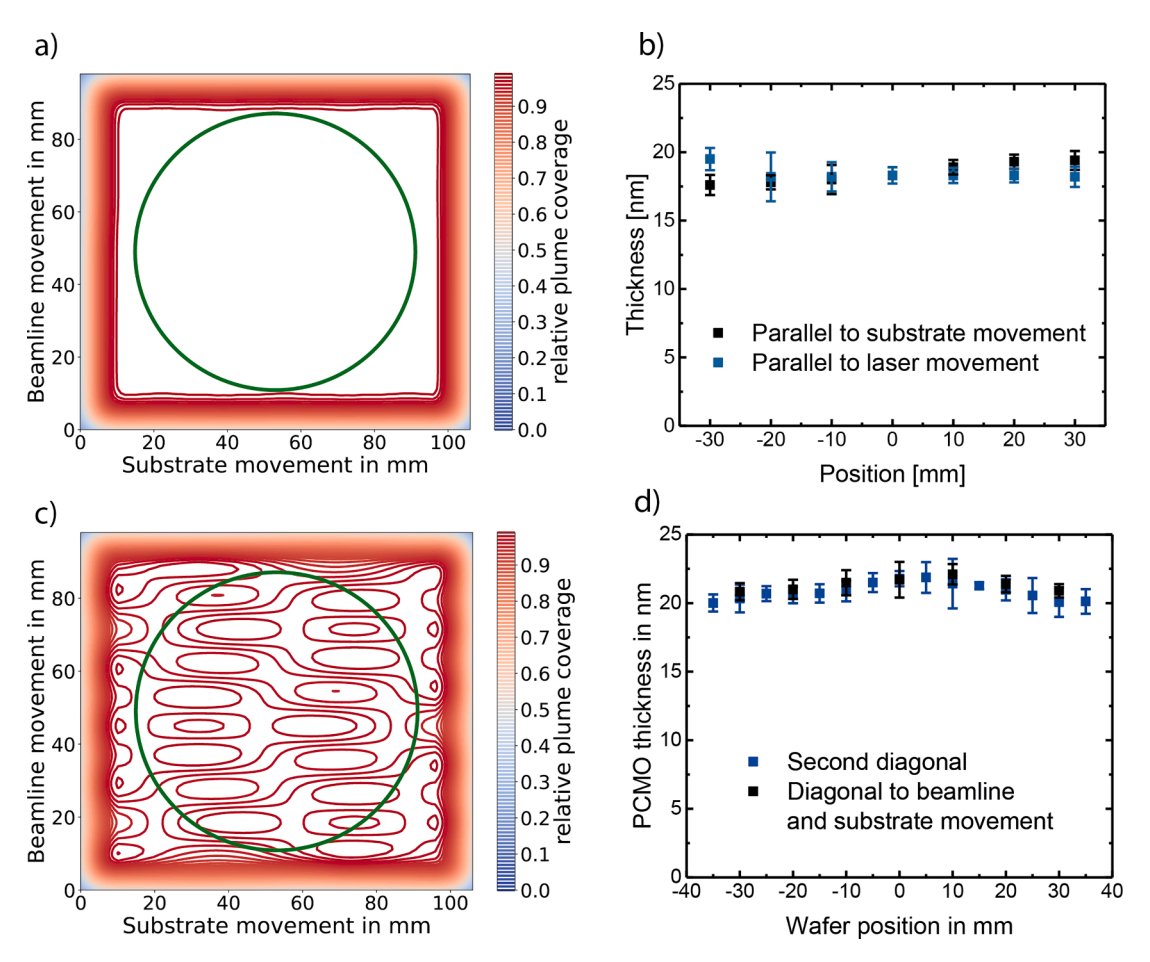


Fig. 3. Simulations of the deposition profiles a) and c) and measured deposition profiles b) and c). a) and b) are a pair and show strategy one, c) and d) are a pair that shows strategy two. To measure the deposition profile for each position, localized XRR measurements and fittings were performed, as exemplary shown in Fig. A.1. a) **Strategy one:** Profile simulation with the parameters (target length 98 mm, substrate length 106 mm, beam line velocity 20 mm/*sec*, target velocity 0.1 mm/*sec*, heat shield 20 mm, target distance 80 mm, q 400, laser 100 Hz and 2100s) standard deviation of the thickness divided by the mean thickness is 0.07 % (taken from the marked circle). **b)** Homogeneous PCMO profile (measured by XRR) along two orthogonal axes across the wafer. Deposition parameters were chosen according to the simulation a) with further process parameters (Fluence 2.5 J/cm², 1 Pa O₂). **c) Strategy two:** Profile simulation with the parameter (target length 98 mm, substrate length 106 mm, beam line speed 5 mm/*sec*, substrate speed 20 mm/*sec*, heat shield 20 mm, target distance 80 mm, q 400, laser 100 Hz and 2000 s). The standard deviation of the thickness divided by the average thickness is 1.5 % (taken from the marked circle). **d)** Homogeneous PCMO profile (measured by XRR) along two orthogonal axes over the wafer. Deposition parameters were chosen according to the simulation a) with further process parameters (Fluence 2.5 J/cm², 1 Pa O₂).

3.3. Development of the simulation strategies for PCMO

The general configurations of the system in Section 3.1 and the software in Section 3.2 have been made using STO as a prototypical complex oxide material. It can be assumed that the general influence of slit size and process pressure on the deposition rate and deposition profile is similar for different oxides. The general configuration for STO and the specific development of the deposition strategies for PCMO ensure that the system is configured to be easily adaptable to different materials.

The software was used to develop strategies to achieve homogeneous deposition for PCMO by selecting an appropriate combination of movement speeds. Since the difficulty of achieving homogeneity increases as the films get thinner, the strategies were developed for a typical layer thickness of 20 nm. Once a working strategy is established for a thin film, it is easier to adapt to a thicker film.

Two strategies were developed. The most straightforward strategy (called here "strategy one") involves moving the beamline quickly while moving the substrate slowly. The simulation software predicts this strategy will have the highest homogeneity, as seen in Fig. 3a. We have confirmed homogeneous PCMO growth for this strategy using XRR measurements, as shown in Fig. 3b. A disadvantage of this strategy is that only multiples of the minimum thickness can be deposited. In the case of Fig 3b, the deposition time was twice the running time of the substrate movement in one direction. Therefore, the minimum thickness for this process parameter is half of the thickness obtained. The minimum thickness is therefore slightly below 10 nm. The minimum thickness cannot be arbitrarily reduced by increasing the substrate speed. If

the substrate speed is too high, inhomogeneous thickness distributions will result due to the larger gaps between the stitched individual plume profiles.

To address the first strategy problem, we used simulation software to develop combinations of fast beamline and substrate movements for a defined number of laser pulses that result in homogeneous deposition. The simulation software indicates that it is possible to identify such combinations. However, the standard deviation within the marked circle is higher than that of the near-perfect simulation for strategy one (Fig. 3a). This strategy also results in a homogeneous layer deposition, which is shown by XRR measurements in Fig. 3d for PCMO. However, it is important to note that the movement speed must be adjusted for different numbers of shots/film thicknesses.

3.4. PLD deposited PCMO based memristive devices on standard Si-wafer

The developed homogeneous deposition process was used to realize PCMO-based memristive devices (switching stack Fig. 4c) on a 4" wafer. Since the switching effect occurs at the PCMO/AlO_x interface, a focus of the fabrication was to achieve a smooth interface between PCMO/AlO_x and AlO_x/Pt. Therefore, both PCMO and AlO_x must possess a low surface roughness. Atomic force microscopy (AFM) showed that the PCMO surface roughness decreases with the oxygen process during the PLD (RMS values [0.2 nm, 0.3 nm, 2.9 nm, 8.3 nm] for [without process gas, 1 Pa, 4 Pa, 10 Pa], background pressure $\sim 10^{-5}$ Pa). The 1 Pa process was chosen for its smooth surfaces. The resulting surface of the PCMO after the deposition on the platinum bottom electrode is shown in the AFM image (Fig. 4a). All the devices shown in this section are from the same

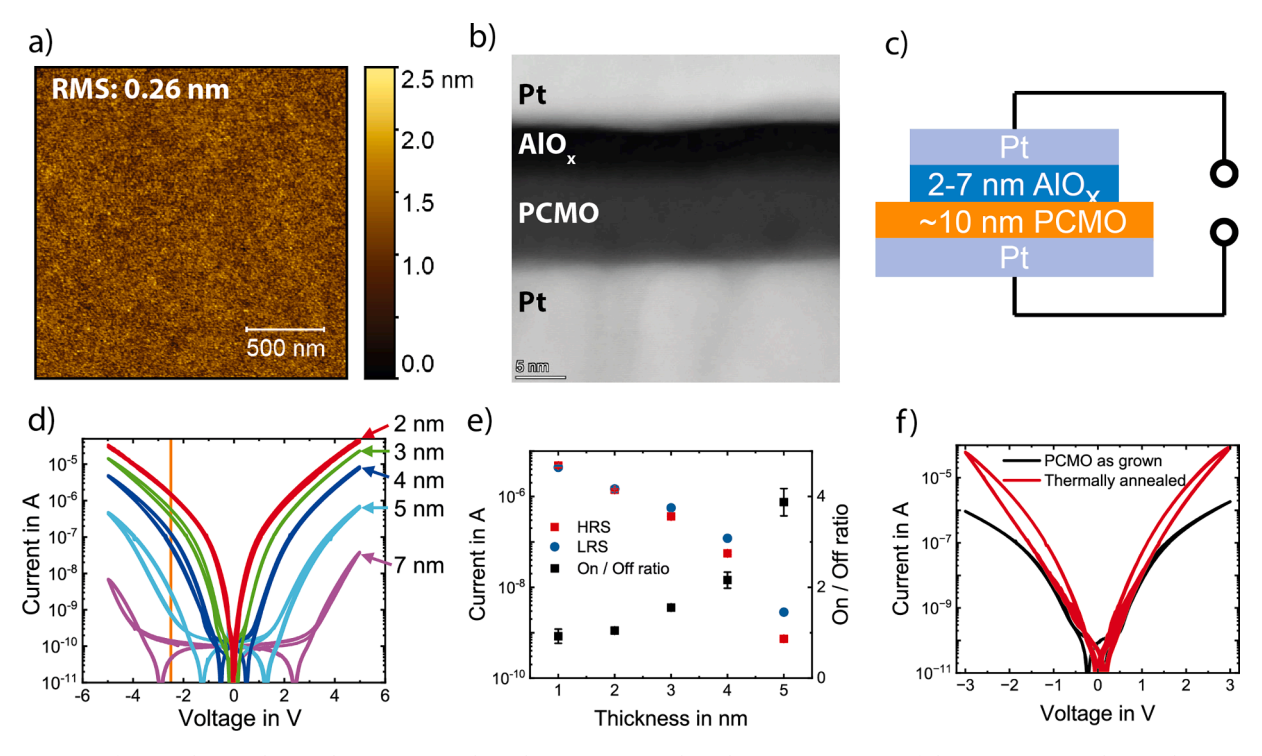


Fig. 4. Integration of LAPLD deposited PCMO layers into area-dependent resistive switching devices. a) AFM scan of about 10 nm PCMO deposited at 1 Pa O_2 on the Pt bottom electrode before dicing and stripping, with an RMS value of 0.26 nm. b) HAADF-STEM cross-section of the whole device stack, with thermally treated PCMO and deposition of 5 nm AlO_x. The platinum electrodes can be seen in light grey. They show the strongest Rutherford scattering because of the high atomic number of Pt (Z(Pt)=78). The PCMO and the AlO_x are sandwiched in between. The PCMO is visible in darker grey (Z(Pr)=59, Z(Mn)=25, Z(Ca)=20), while the AlO_x does not show strong scattering because of the low atomic number of its constituents (Z(O)=8, Z(Al)=13)) and is therefore black. c) Schematic device cross section. d) AlO_x thickness dependence of IV curves of devices with non-annealed PCMO and a constant pad size of 50 μ m x 50 μ m. e) Extracted of the cycles of Figure d) at the orange marked voltage of -2.5 V. The average current levels of the sweep branch into the negative voltage direction (HRS) and the returning sweep branch back to the positive voltage direction (LRS). 7 nm are neglected since here the capacitive charging is too high for a read out at 2.5 V. Further, Figure e) shows also their calculated On/Off ratio. f) Displays the difference between the IV-loops of a 50 μ m x 50 μ m, 3 nm AlO_x device with and without thermal treatment of the PCMO.

wafer, deposited with the movement strategy two (Fig. 3c+d) and by 50,000 shots, which lead to a PCMO layer of around 10 nm (Fig. 4b). Inductively coupled plasma mass spectrometry (ICP-MS) on a similarly processed wafer (same pressure, fluence, slit settings) showed a homogeneous stoichiometry for neighboring pieces with average values of $Pr_{0.81}Ca_{0.25}Mn_{0.94}$ (Fig. A.5).

The RF sputter deposition of the aluminum oxide in a reactive gas atmosphere (3:2 (Ar:O₂) flow rate mixture) resulted in smooth oxide layers (RMS 0.2 nm - Fig. A.3). X-ray photoelectron spectroscopy (XPS) on the AlO_x surface shows plasmonic loss features of the Al2s and Al2p peak as well as a mixed contribution of metal and oxide peak at the Al2p level (Fig. A.4). It is therefore considered as suboxide. The XPS measurement was performed immediately after the deposition of the AlO_x by in-situ transfer to avoid the influence of atmospheric oxygen. The whole device stack can be seen in the high-angle annular dark-field-scanning transmission electron microscope (HAADF-STEM) images (Fig. 4b).

The current-voltage (IV) loops of devices with different AlOx thicknesses are compared in Fig. 4 d and e. The IV curve exhibits a hysteresis at an oxide thickness of 3 nm. The ratio of the current of the low resistive state (LRS) and the high resistive state (HRS) ratio increases with increasing AlO_x thickness (Fig. A.4 e) from 2 nm AlO_x (1.07 \pm 0.13) over 3 nm (1.53 \pm 0.19) and 4 nm (2.20 \pm 0.42) up to 5 nm (3.90 \pm 0.89) until the resistance becomes too high and capacitive charging dominates, as seen for the 7 nm layer. Sweep voltages of 5 V are required to exhibit hysteresis, as can be seen when comparing 3 and 4 V (Fig. A.6). 3 V is unsuitable for hysteresis and the IV loop opening at 4 V is insignificant small. Fig. A.8 shows the stability of the LRS of the 5 nm AlO_x sample. The LRS is stable for 6 min. It shows serious decay after 1 hour and 13 min and a nearly complete decay after 21 h. The timescale of the retention is common for area-dependent devices. The device's endurance is shown in Fig. A.9, using IV-cycles. It shows a constant On/Off ratio for 100 cycles and a complete failure after 579 cycles. Degradation over the cycles is leading to increased LRS and HRS resistances. The IVloops show good reproducibility, as seen from the low device-to-device variation (Fig. A.10).

All these devices in Fig. 4 d have no thermal treatment of the PCMO and are therefore compatible with the back end of line processing in standard CMOS technology. Further thermal treatment at 923 K for 2 min of the as-deposited amorphous PCMO causes crystallization (Fig. A.2). This reduces the resistance and switching voltage and increases the ratio between the LRS and HRS, as can be seen in Fig. 4 f. Both types of devices, with amorphous and with crystalline PCMO, show area-dependent scaling of the HRS and LRS, as can be seen in the double logarithmic current-area plot (Fig. A.7). The slope of the linear fit is close to 1.

4. Conclusions

In this study, we addressed the issue of plume broadening for largearea pulsed laser deposition using a slit system. The influence of the slit system and deposition pressure has been analyzed—this knowledge

parameterized simulation software and developed two strategies showing homogeneous layers. One strategy is moving the beamline quickly while moving the substrate slowly, which showed the highest homogeneity in the simulation. The other strategy is to move both the beamline and the substrate fast while finding an appropriate combination of both speeds for a given number of laser shots. Both strategies were experimentally verified, producing a homogeneous PCMO thin film on 4" wafers. This process produced PCMO/AlO_x-based devices with well-defined, smooth interfaces. The devices show area-dependent resistive switching, for amorphous and for crystalline PCMO. The influence of the aluminum oxide thickness on the switching shows that the IV loop starts to exhibit a hysteresis for AlO_x thicknesses ≥ 3 nm. An increase in AlOx thickness leads to an increase in resistance and capacitive charging. An additional thermal treatment reduces the resistance and switching voltage and increases the ratio between low and high resistive states. Devices without thermal treatment of the PCMO are compatible with the back-end-of-line processing (BEOL) of standard CMOS technology

CRediT authorship contribution statement

M. Buczek: Writing – original draft, Visualization, Methodology, Investigation, Formal analysis, Data curation, Conceptualization. M. Pohlmann: Writing – review & editing, Visualization, Software, Methodology, Investigation, Formal analysis, Data curation, Conceptualization. Z. Liu: Visualization, Investigation, Formal analysis, Data curation. Z. Moos: Writing – review & editing, Investigation. A. Gutsche: Writing – review & editing, Validation. P. Cao: Visualization, Investigation, Formal analysis, Data curation. J. Mayer: Supervision. W. Stein: Writing – review & editing, Supervision, Project administration, Methodology, Conceptualization. R. Dittmann: Writing – review & editing, Validation, Supervision, Project administration, Funding acquisition, Conceptualization.

Declaration of competing interest

The authors declare that they have no known competing financial interests or personal relationships that could have appeared to influence the work reported in this paper.

Data availability

Data will be made available on request.

Acknowledgments

This work was funded by the Federal Ministry of Education and Research project NEUROTEC (Grants No 16ME0398K and No 16ME0399) and NeuroSys (03ZU1106AB).

Appendix

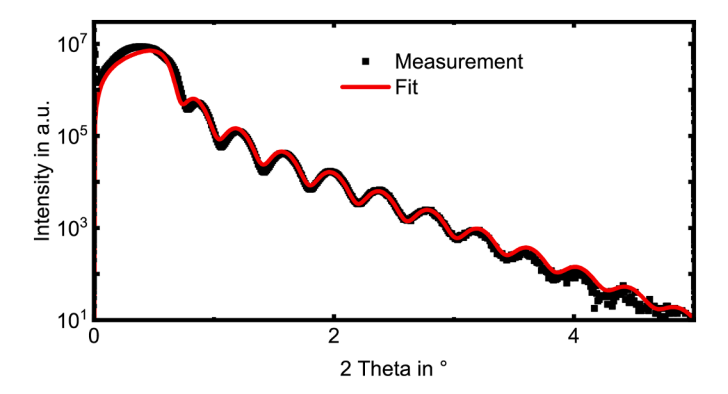


Fig. A.1. Example of the fitting of XRR-data, as done for Fig 3 b and d. The XRR data shown are from Fig 3 d (measurement: second diagonal at 20 mm). The fitting led to the following material parameters (PCMO thickness: 21.0 nm, surface roughness: 0.6 nm, interface roughness: 0.7 nm, density: 4.6 g/cm³). The fitting was performed by the program GenX 3.6.22 [1]. The stack was simulated using a two-layer model of PCMO and SiO₂. For the bottom layer of SiO₂, a density of 2.65 g/cm³ was assumed. The free parameters of the fit are the interface roughness, the surface roughness, the density of PCMO, and the thickness. The count intensity was manually chosen according to the low angle count rate. The fit was done by prioritizing the thickness by matching the oscillation periodicity. The measurement was performed with a Bruker D8 diffractometer with a Cu K-alpha source and Bragg-Brentano geometry. A 2 mm circular nozzle was used to spatially confine the beam.

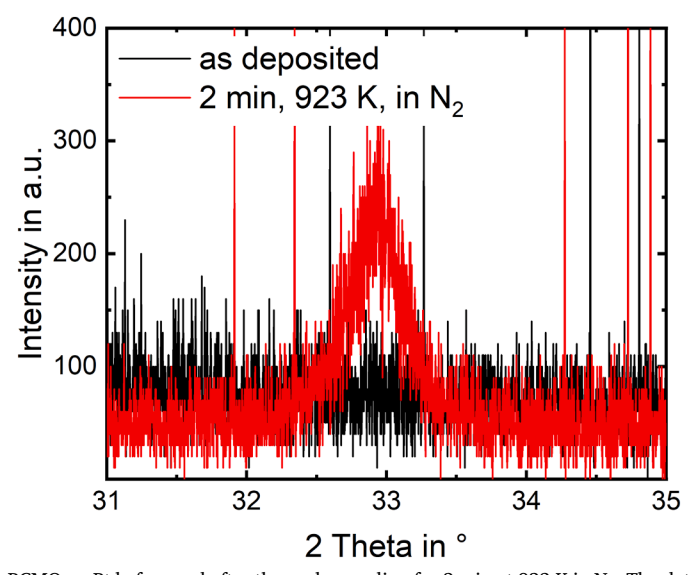


Fig. A.2. GI-XRD measurement of 95 nm PCMO on Pt before and after thermal annealing for 2 min at 923 K in N_2 . The data clearly shows the appearance of a Bragg reflection and, therefore, the crystallization of the previous amorphous PCMO layer. The broad peak covers in the case of a perfect crystalline PCMO with orthorhombic symmetry (space group Pnma (62)) the (200), (121) (1–21), (12–1), (12–1) and (002) orientation [2,3]. A pseudo cubic notation would represent them by the (110) orientation. The measurements have been done around these peaks because they have the highest structure factor |F|. The measurement was done with a Bruker D8 diffractometer with a Cu K-alpha source and Bragg-Brentano geometry. The constant incidence angle ω was set to 0.4° .

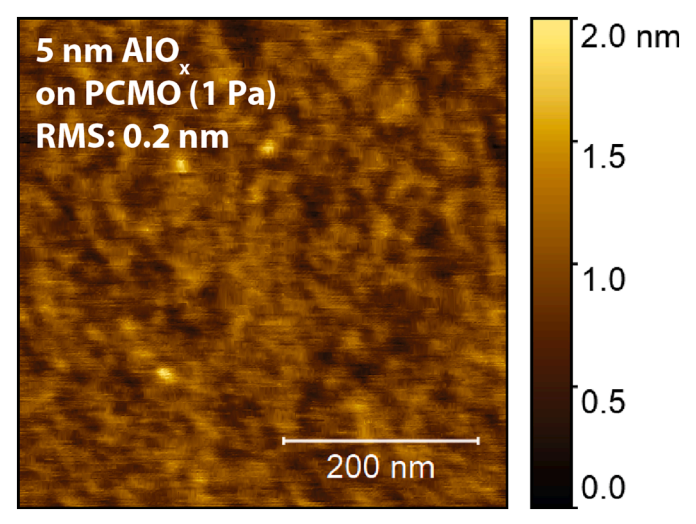


Fig. A.3. Atomic force microscopy images show the surface of the 5 nm AlO_x sputter deposited on the, in Section 3.3 used, PCMO deposited at 1 Pa on Pt.

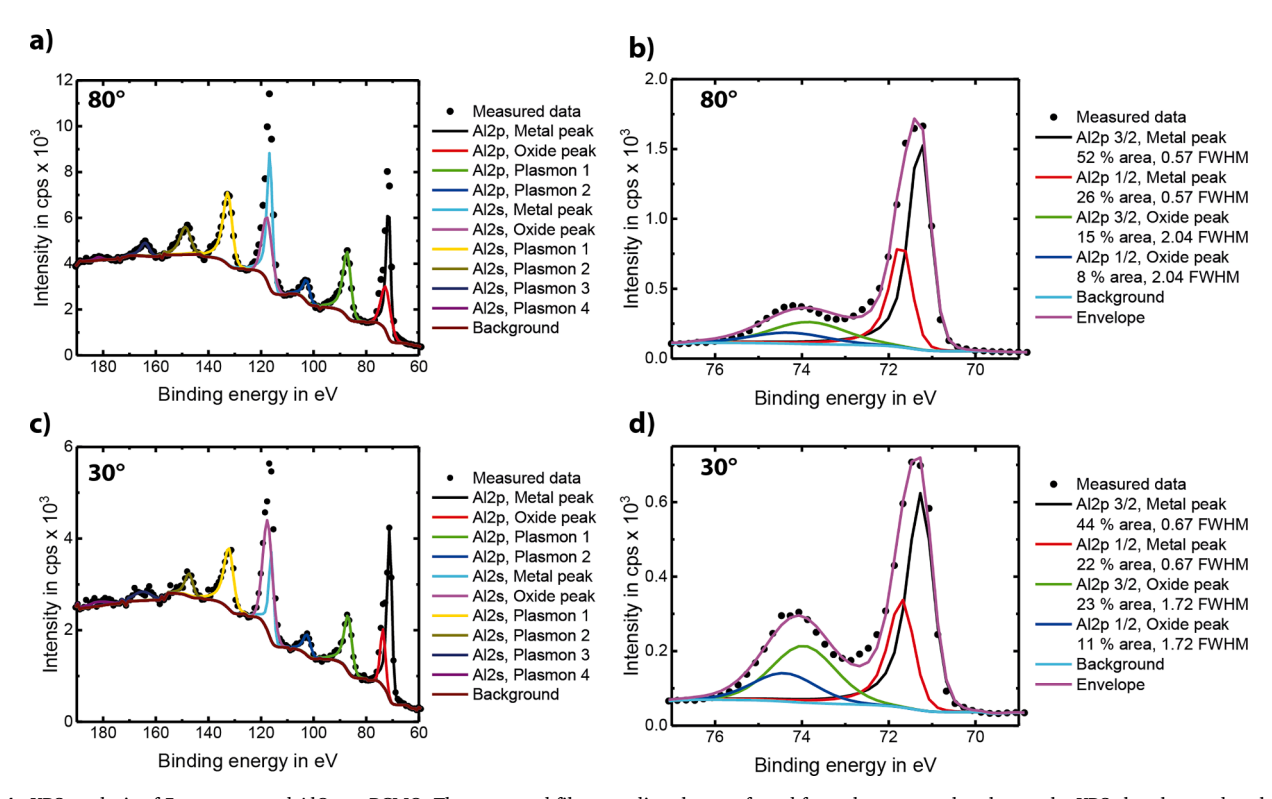


Fig. A.4. XPS-analysis of 5 nm sputtered AlO_x on PCMO. The sputtered film was directly transferred from the sputter chamber to the XPS chamber under ultra-high vacuum conditions. The sputter deposition was done in a reactive gas atmosphere at 2 Pa with a gas mixture of argon and oxygen (3:2 (Ar:O₂) flow rate mixture) with alternating current (RF magnetron at 200 W), a target substrate distance of around 10 mm and a sputtering time of 45 s. The XPS analysis was done at a PHI 5000 Versa Probe, with a monochromatic Al Kα x-ray source for photoelectron excitation and an argon gun, and an electron gun for charge neutralization. The hemispherical analyzer used a path energy of 187.85 eV for the survey scan a) and c) and 23.5 eV for the Al2p peak scans b) and d). All spectra are from the same point and have been checked for reproducibility at a second point at the sample surface. Spectra a) and b) were taken at a detector angle of 80° from the surface plane and are therefore more depth sensitive than the spectra c) and d), which were taken at a surface sensitive angle of 30° For the data analysis, the program CasaXPS Version 2.3.24PR.0 was used. All spectra had been charge corrected by setting the aliphatic carbon peak to 284.8 eV. To fit the background a Shirley background was used. The metallic peaks had been fitted by an asymmetric peak shape of ST(1.3)LA(1,1.63,143) as recommended by [4]. The same peak shape was used to identify the asymmetric plasmon peak in the survey scans. The oxide peaks had been fitted by GL(30), a symmetric product function of Gaussian and Lorentzian contribution, with a mixing ratio of 70:30. The following constraints were used for fitting the Al2p spectra b) and d). As expected from the spin-orbit coupling, the area ratio for the 1/2 and 3/2 metal peaks and oxide peaks had been constrained with a 1:2 ratio. The FWHM of the corresponding multiplets are constrained to be equal. Further, the energy difference of both multiplets had been assumed to be 0.44 eV, as recommended by [4]. In a) and c), plasmonic excitations can be identified, which are associated with electronic oscillation in the conduction band [5] and therefore a sign of metallic contribution. The peak fitting on the Al2p spectra shows an increase of the oxide peak for the surface sensitive measurement from signal area contribution of b) 23 % at an 80° take-off angle to d) 34 % at 30° The increased oxygen content at the surface could be explained by an additional oxidation reaction in the reactive gas atmosphere at the sample surface after the sputter deposition.

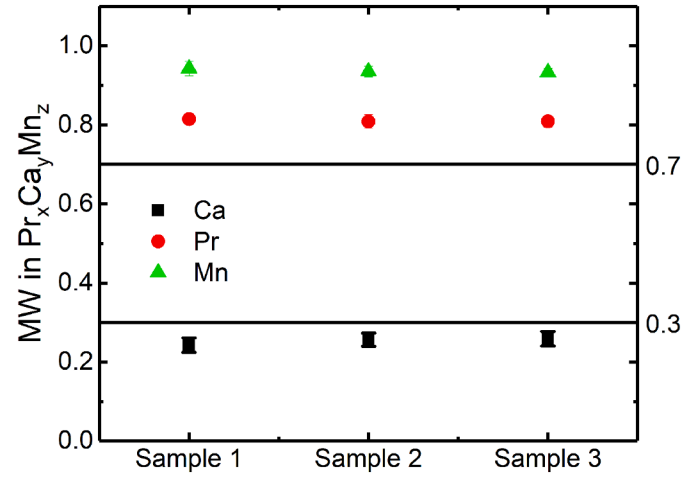


Fig. A.5. Stoichiometry measurement of PCMO by ICP-MS. The PCMO was deposited on the Pt coated thermally oxidized 4'' Si Wafer with the following stack: 20 nm Pt/ 5 nm Ta/ ~ 430 nm SiO₂/Si. The deposition parameters were: fluence 2.5 J/cm², 1 Pa O₂ process gas pressure, 20 mm heat slit opening, 4 mm target slit opening, laser repetition rate: 100 Hz, laser shots: 212 000, target-rotation: 100 rpm, beamline movement from 4 till 104 mm with 20 mm/sec, substrate movement in step mode with 0.25 mm step size at each turning point of the beamline, background pressure $\sim 10^{-5}$ Pa. The wafer was diced into 1×1 cm pieces. Three neighboring pieces had been taken from the homogeneous region. The acid digestion was done by cooking for 2 h at 323 K in 3 ml HNO₃ and 1 ml H₂O₂. Three aliquots in 20:1 and 10:1 dilution were taken from each sample for analysis. The ICP-MS was done in an Agilent-8900 by comparison with element standards.

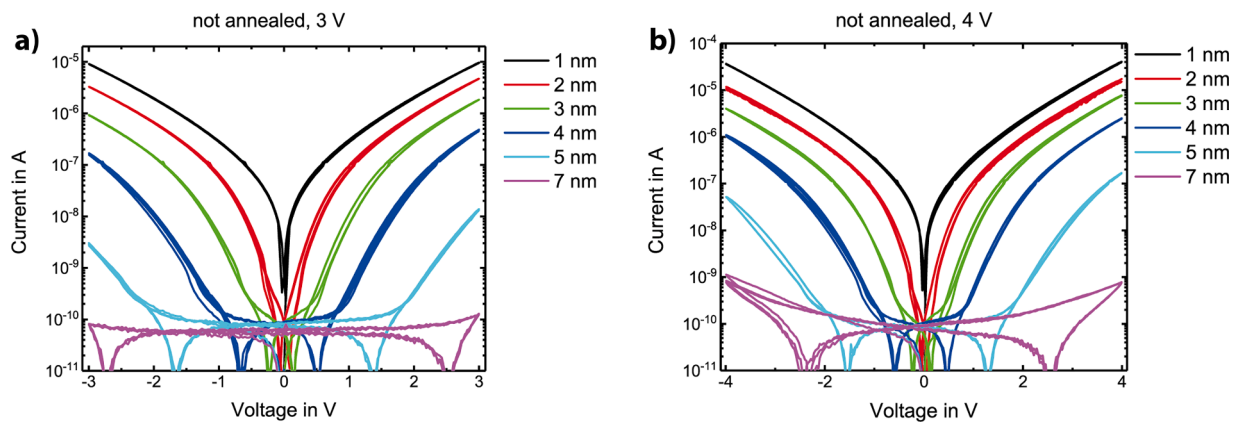


Fig. A.6. AlO_x thickness dependence of IV-loops for the not annealed PCMO devices with a pad size of 50 μ m x 50 μ m for different applied maximal voltages a) 3 V, b) 4 V. The IV-loops do not show a pronounced hysteresis comparing to IV-loops with a peak voltage of 5 V (Fig. 4d). The IV loops were measured with stepping rates of 30 mV and holding times of 20 ms at each voltage step, which led to an effective sweep rate of 1.5 V/s.

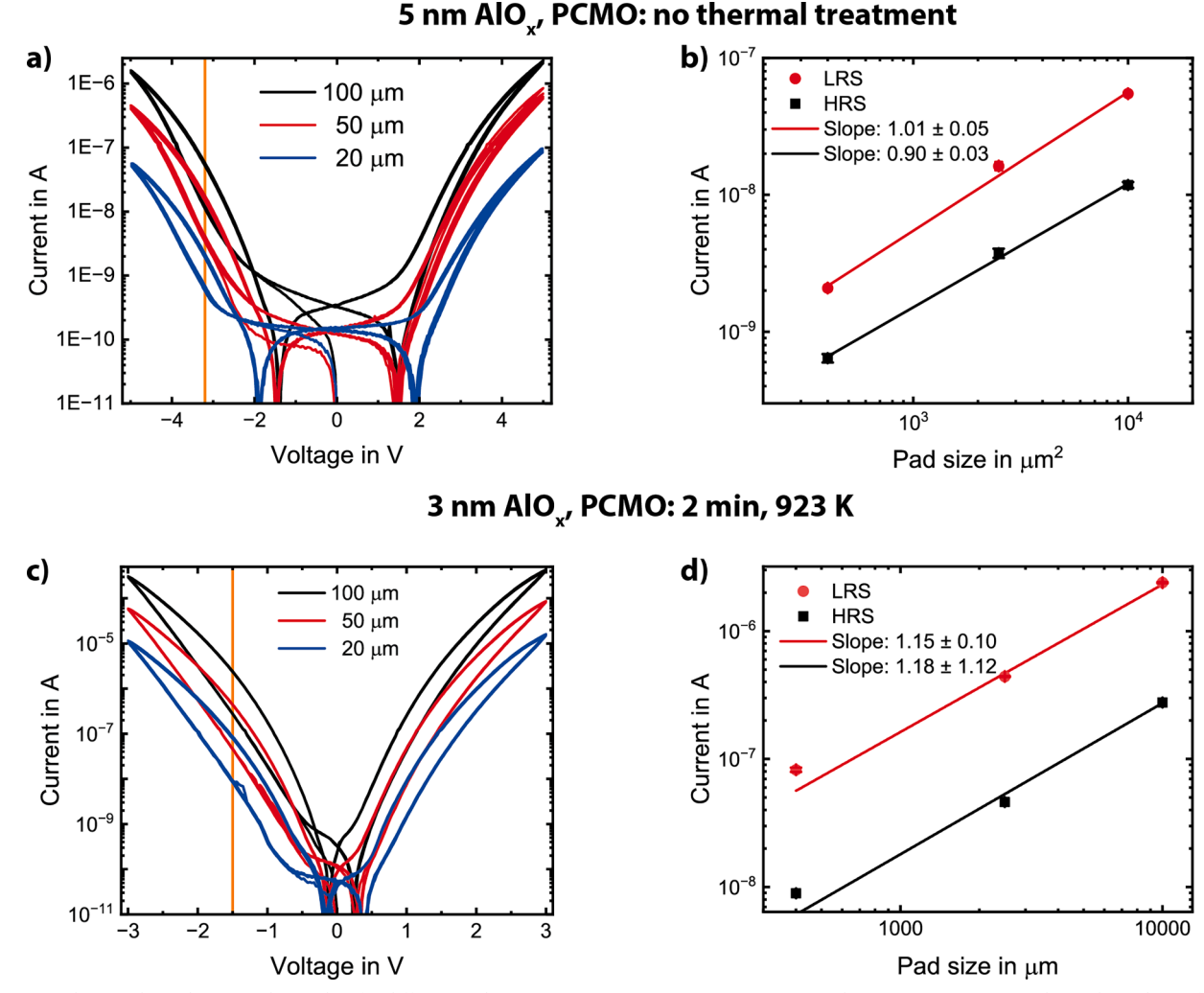


Fig. A.7. a) and c) are the IV-loops (each 3 cycles) for different pad sizes ($20 \, \mu m \, x \, 20 \, \mu m$), ($50 \, \mu m \, x \, 50 \, \mu m$), and ($100 \, \mu m \, x \, 100 \, \mu m$). a) Shows the IV-loop of a sample without thermal treatment of the PCMO and with 5 nm AlO_x. and c) displays the IV loops of thermally treated ($2 \, min$, at $923 \, K \, in \, N_2$) PCMO with 3 nm AlO_x. b) and d) plot the HRS and LRS from the IV-loops of a) and c). The values are taken at the orange-marked voltages. The linear fit in the double logarithmic plot checks the area dependence. The fitting results of the slope are written in the legend.

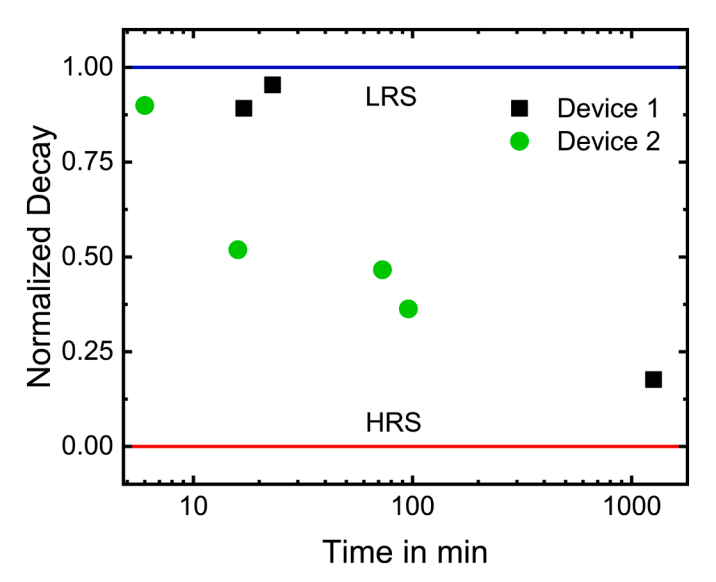


Fig. A.8. The normalized decay of the LRS was measured on two devices with a $(50 \ \mu m \ x \ 50 \ \mu m)$ pad, 5 nm AlO_x, and PCMO without thermal treatment. After different waiting times, the values were extracted at $-3.2 \ V$ from IV sweeps. The device was set to the LRS for each time tested by three consecutive 5 V sweeps. The reference for the HRS is measured after the device has been set to the HRS by three consecutive $+5 \ V$ sweeps.

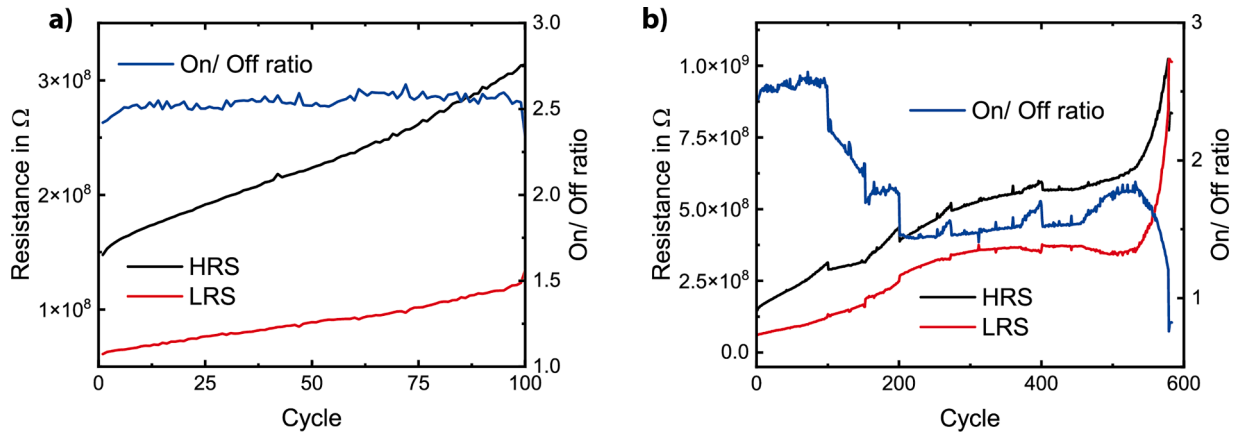
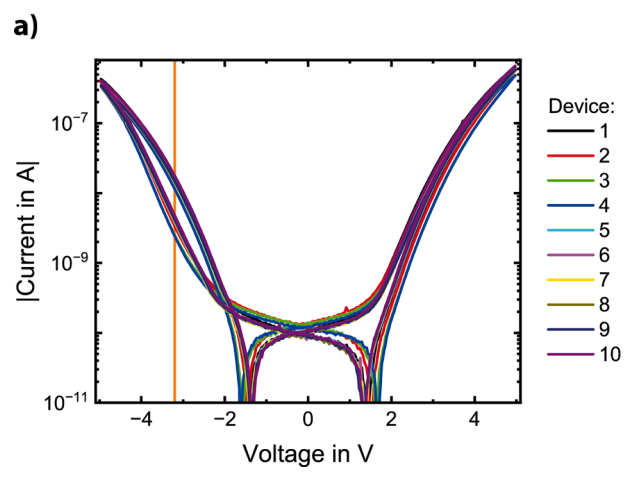


Fig. A.9. Endurance measurements by IV-loops on the sample with 5 nm ${\rm AlO}_{\rm X}$ and amorphous PCMO. The first 100 cycles a) show a constant On/Off ratio while the HRS and LRS slowly increase. b) shows all 583 cycles, with the device failure after 579 cycles. The degradation of the devices led to a continuous increase of the resistance till LRS and HRS were indistinguishable. The graph had been stacked together from four measurement sets—cycle 1 till 100, 101 till 200, 201 till 400, and 401 till 583. Since the IV-loops have charging contributions during sweeping, small discontinuities can be seen at the merging points (cycles 101, 201, and 401). All The IV-loops were done without holding time at the voltage steps and with a step width of 100 mV to reduce the degradation by a reduced measurement time. The pure measurement time of the Keithley 2611A source meter delayed by communication with a LabView user interface led to a sweep rate of around 3.3 V/s. The values were extracted from the IV-loops at -4 V.



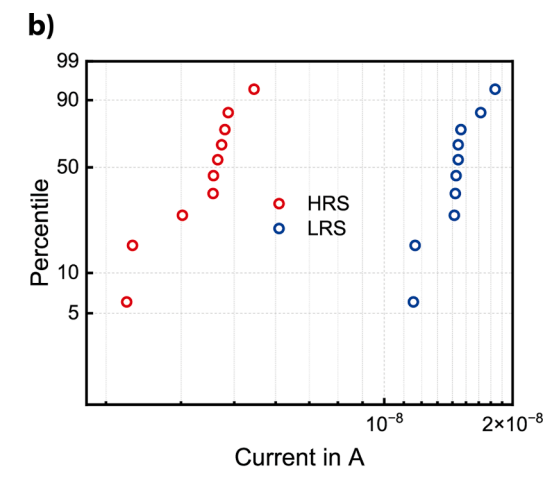


Fig. A.10. Device-to-device variation measured on ten different devices with $(50 \, \mu m \times 50 \, \mu m)$ pad, $5 \, nm$ AlO_x, and amorphous PCMO. a) Comparison of the IV loops. It shows one cycle per device. The chosen device was initialized by at least one previous cycle. b) shows the quantile probability plot of the HRS and LRS extracted from a) at the voltage marked in orange. The double logarithmic reciprocal y scale was chosen in the style of a Weibull plot. The approximation of the percentile probability was done using the Blom method.

References

- [1] D.V. Christensen, R. Dittmann, B. Linares-Barranco, A. Sebastian, M.Le Gallo, A. Redaelli, S. Slesazeck, T. Mikolajick, S. Spiga, S. Menzel, I. Valov, G. Milano, C. Ricciardi, S.J. Liang, F. Miao, M. Lanza, T.J. Quill, S.T. Keene, A. Salleo, J. Grollier, D. Marković, A. Mizrahi, P. Yao, J.J. Yang, G. Indiveri, J.P. Strachan, S. Datta, E. Vianello, A. Valentian, J. Feldmann, X. Li, W.H.P. Pernice, H. Bhaskaran, S. Furber, E. Neftci, F. Scherr, W. Maass, S. Ramaswamy, J. Tapson, P. Panda, Y. Kim, G. Tanaka, S. Thorpe, C. Bartolozzi, T.A. Cleland, C. Posch, S. C. Liu, G. Panuccio, M. Mahmud, A.N. Mazumder, M. Hosseini, T. Mohsenin, E. Donati, S. Tolu, R. Galeazzi, M.E. Christensen, S. Holm, D. Ielmini, N. Pryds, 2022 roadmap on neuromorphic computing and engineering, Neuromorph. Comput. Eng. 2 (2022), https://doi.org/10.1088/2634-4386/ac4a83.
- [2] S. Bagdzevicius, K. Maas, M. Boudard, M. Burriel, .K. Maas, M. Boudard, M. Burriel, Interface-type resistive switching in perovskite materials, J. Electroceram. 39 (2022) 235–287, https://doi.org/10.1007/978-3-030-42424-4 11.
- [3] R. Dittmann, S. Menzel, R. Waser, Nanoionic memristive phenomena in metal oxides: the valence change mechanism, Adv. Phys. 70 (2021) 155–349, https://doi. org/10.1080/00018732.2022.2084006.
- [4] S. Menzel, U. Böttger, M. Wimmer, M. Salinga, Physics of the switching kinetics in resistive memories, Adv. Funct. Mater. 25 (2015) 6306–6325, https://doi.org/ 10.1002/ADFM.201500825.
- [5] S. Menzel, M. Waters, A. Marchewka, U. Böttger, R. Dittmann, R. Waser, S. Menzel, A. Marchewka, U. Böttger, R. Waser, M. Waters, R. Dittmann, Origin of the ultranonlinear switching kinetics in oxide-based resistive switches, Adv. Funct. Mater. 21 (2011) 4487–4492, https://doi.org/10.1002/ADFM.201101117.
- [6] A. Gutsche, S. Siegel, J. Zhang, S. Hambsch, R. Dittmann, Exploring areadependent Pr_{0.7}Ca_{0.3}MnO₃-based memristive devices as synapses in spiking and artificial neural networks, Front. Neurosci. 15 (2021) 661261, https://doi.org/ 10.3389/FNINS.2021.661261/BIBTEX.
- [7] Z. Liao, P. Gao, Y. Meng, H. Zhao, X. Bai, J. Zhang, D. Chen, Electroforming and endurance behavior of Al/Pr_{0.7}Ca_{0.3}MnO₃/Pt devices, Appl. Phys. Lett. 99 (2011) 113506. https://doi.org/10.1063/1.3638059/923350.
- [8] Z.L. Liao, Z.Z. Wang, Y. Meng, Z.Y. Liu, P. Gao, J.L. Gang, H.W. Zhao, X.J. Liang, X. D. Bai, D.M. Chen, Categorization of resistive switching of metal- Pr_{0.7}Ca_{0.3}MnO₃-metal devices, Appl. Phys. Lett. 94 (2009) 253503, https://doi.org/10.1063/13159471/131435
- [9] Y. Lei, H. Zeng, W. Luo, Y. Shuai, X. Wei, N. Du, D. Bürger, I. Skorupa, J. Liu, O. G. Schmidt, W. Zhang, H. Schmidt, Ferroelectric and flexible barrier resistive switching of epitaxial BiFeO₃ films studied by temperature-dependent current and capacitance spectroscopy, J. Mater. Sci.: Mater. Electron. 27 (2016) 7927–7932, https://doi.org/10.1007/S10854-016-4784-Y/FIGURES/5.
- [10] M. Coll, J. Fontcuberta, M. Althammer, M. Bibes, H. Boschker, A. Calleja, G. Cheng, M. Cuoco, R. Dittmann, B. Dkhil, I. El Baggari, M. Fanciulli, I. Fina, E. Fortunato, C. Frontera, S. Fujita, V. Garcia, S.T.B. Goennenwein, C.G. Granqvist, J. Grollier, R. Gross, A. Hagfeldt, G. Herranz, K. Hono, E. Houwman, M. Huijben, A. Kalaboukhov, D.J. Keeble, G. Koster, L.F. Kourkoutis, J. Levy, M. Lira-Cantu, J. L. MacManus-Driscoll, J. Mannhart, R. Martins, S. Menzel, T. Mikolajick, M. Napari, M.D. Nguyen, G. Niklasson, C. Paillard, S. Panigrahi, G. Rijnders, F. Sánchez, P. Sanchis, S. Sanna, D.G. Schlom, U. Schroeder, K.M. Shen, A. Siemon, M. Spreitzer, H. Sukegawa, R. Tamayo, J. van den Brink, N. Pryds, F.M. Granozio, Towards oxide electronics: a roadmap, Appl. Surf. Sci. 482 (2019) 1–93, https://doi.org/10.1016/J.APSUSC.2019.03.312.

- [11] Y.Z. Chen, N. Bovet, F. Trier, D.V. Christensen, F.M. Qu, N.H. Andersen, T. Kasama, W. Zhang, R. Giraud, J. Dufouleur, T.S. Jespersen, J.R. Sun, A. Smith, J. Nygård, L. Lu, B. Büchner, B.G. Shen, S. Linderoth, N. Pryds, A high-mobility two-dimensional electron gas at the spinel/perovskite interface of γ-Al₂O₃/SrTiO₃, Nat. Commun. 2013 (4) (2013) 1–6, https://doi.org/10.1038/ncomms2394, 1 4.
- [12] M. Spreitzer, R. Egoavil, J. Verbeeck, D.H.A. Blank, G. Rijnders, Pulsed laser deposition of SrTiO₃ on a H-terminated Si substrate, J. Mater. Chem. C. Mater. 1 (2013) 5216–5222, https://doi.org/10.1039/C3TC30913D.
- [13] C. Baeumer, C. Schmitz, A. Marchewka, D.N. Mueller, R. Valenta, J. Hackl, N. Raab, S.P. Rogers, M.I. Khan, S. Nemsak, M. Shim, S. Menzel, C.M. Schneider, R. Waser, R. Dittmann, Quantifying redox-induced Schottky barrier variations in memristive devices via in operando spectromicroscopy with graphene electrodes, Nat. Commun. 2016 (7) (2016) 1–7, https://doi.org/10.1038/ncomms12398, 1 7.
- [14] V. Sivakumar, S. Kumar, C. Ross, T. Mukai, T. Fujita, S. Tsukui, J. Zhang, J. M. McGraw, D.H.A Blank, M. Dekkers, G. Rijnders, Pulsed laser deposition in Twente: from research tool towards industrial deposition, J Phys D Appl Phys 47 (2013) 034006, https://doi.org/10.1088/0022-3727/47/3/034006.
- [15] J.A. Greer, History and current status of commercial pulsed laser deposition equipment, J. Phys. D. Appl. Phys. 47 (2013) 034005, https://doi.org/10.1088/ 0022-3727/47/3/034005.
- [16] N.A. Shepelin, Z.P. Tehrani, N. Ohannessian, C.W. Schneider, D. Pergolesi, T. Lippert, A practical guide to pulsed laser deposition, Chem. Soc. Rev. 52 (2023) 2294–2321, https://doi.org/10.1039/D2CS00938B.
- [17] J.A. Greer, M.D. Tabat, M.D. Tabat, Large-area pulsed laser deposition: techniques and applications, J. Vacuum Sci. Technol. A 13 (1995) 1175–1181, https://doi. org/10.1116/1.579857
- [18] J.A. Greer, M.D. Tabat, C. Lu, Future trends for large-area pulsed laser deposition, Nucl. Instrum. Methods Phys. Res. B 121 (1997) 357–362, https://doi.org/ 10.1016/S0168-583X(96)00434-X.
- [19] N. Pryds, B. Toftmann, J.B. Bilde-Sørensen, J. Schou, S. Linderoth, Thickness determination of large-area films of yttria-stabilized zirconia produced by pulsed laser deposition, Appl. Surf. Sci. 252 (2006) 4882–4885, https://doi.org/10.1016/ J.APSUSC.2005.07.145.
- [20] S. Boughaba, M. Islam, J.P. McCaffrey, G.I. Sproule, M.J. Graham, Ultrathin Ta₂O₅ films produced by large-area pulsed laser deposition, Thin. Solid. Films. 371 (2000) 119–125, https://doi.org/10.1016/S0040-6090(00)00982-2.
- [21] Z. Vakulov, D. Khakhulin, E. Zamburg, A. Mikhaylichenko, V.A. Smirnov, R. Tominov, V.S. Klimin, O.A. Ageev, Towards scalable large-area pulsed laser deposition, Materials. (Basel) 14 (2021) 4854, https://doi.org/10.3390/ MA14174854/S1.
- [22] S. Sakai, M. Takahashi, K. Motohashi, Y. Yamaguchi, N. Yui, T. Kobayashi, Largearea pulsed-laser deposition of dielectric and ferroelectric thin films, J. Vacuum Sci. Technol. A 25 (2007) 903–907, https://doi.org/10.1116/1.2748808.
- [23] A. Ojeda-G-P, C.W. Schneider, M. Döbeli, T. Lippert, A. Wokaun, Angular distribution of species in pulsed laser deposition of La_xCa_{1-x}MnO₃, Appl. Surf. Sci. 336 (2015) 150–156, https://doi.org/10.1016/J.APSUSC.2014.10.089.
- [24] C. Pithan, Y. Iida, J. Dornseiffer, A. Tsubouchi, R. Waser, Oxygen nonstoichiometry and electrical transport properties of Pr_{1-x}Ca_xMnO₃ ceramics, J. Eur. Ceram. Soc. 42 (2022) 7049–7062, https://doi.org/10.1016/J.JEURCERAMSOC.2022.08.006.
- [25] L. Amaral, A.M.R. Senos, P.M. Vilarinho, Sintering kinetic studies in nonstoichiometric strontium titanate ceramics, Mater. Res. Bull. 44 (2009) 263–270, https://doi.org/10.1016/J.MATERRESBULL.2008.06.002.